Correlative Electron Energy Loss Spectroscopy and Cathodoluminescence Spectroscopy on Three-Dimensional Plasmonic Split Ring Resonator

Bicket, Isobel; McMaster University, Department of Materials Science and Engineering

Bellido, Edson; McMaster University, Department of Materials Science and Engineering

Meuret, Sophie; FOM-instituut AMOLF, Center for Nanophotonics

Polman, Albert; FOM-instituut AMOLF, Center for Nanophotonics

Botton, G A; McMaster University, Canada, Department of Materials Science and Engineering

Keywords: Electron energy loss spectroscopy, Cathodoluminescence, Surface plasmon resonance, Split ring resonator, Correlative spectroscopy, 3D nanostructure

Abstract

We present the surface plasmon resonance modes in three-dimensional upright split ring resonators as studied by correlative cathodoluminescence spectroscopy (CL) in a scanning electron microscope and electron energy loss spectroscopy (EELS) in a transmission electron microscope. We discuss the challenges inherent in studying the plasmon modes of a three-dimensional nanostructure and how meeting these challenges benefits from the complementary use of EELS and SEM-CL. With the use of EELS we detect a strong first order mode in the split ring resonator; with comparison to simulations, we are able to identify this as the well-known magnetic dipole moment of the split ring resonator. Combining the EELS spectra with SEM-CL on the same structure reveals the higher-order modes present in this three-dimensional nanostructure, which we link to the coupling and hybridization of rim modes present in the two upright hollow pillars of the split ring.

Introduction

Surface plasmons are collective oscillations of electron density on the interface between conducting media and insulating dielectrics. Confining these oscillations within a nanostructure discretizes them into localized resonance modes: surface plasmon resonances (SPR). SPRs present in sub-wavelength structures provide a way to engineer the properties of light, giving the material unique optical properties difficult to obtain in natural materials; materials such as these are known as metamaterials [1], [2].

The split ring resonator (SRR) is a well-known example of a sub-wavelength structure used as a building block for metamaterials, giving the metamaterial a negative permeability and thus a negative refractive index [2]–[4]. The SRR produces this property because of its structure: an oscillating SPR mode produces a magnetic dipole moment through the arms of the split ring (Figure 1). The wavelength of light with which the SRR interacts is determined by the structure size; to achieve operation in the infrared or visible regime, the SRR must be scaled down to the nanoscale. Scaling down of the SRR involves increasingly complex fabrication techniques: from macroscale assembly of millimeter size SRRs [5]; to photolithography on the micrometer scale [6], [7]; to electron beam lithography for nanoscale structures [8]–[11].

On the nanoscale, most studies concern the planar SRR, due to the relative ease of fabrication compared to an upright, three-dimensional SRR. With the planar SRR, the magnetic dipole moment is normal to the surface (Figure 1a), making it difficult to couple this magnetic moment directly with incoming light. Fabrication of an upright split ring resonator makes this coupling much easier because of the in-plane magnetic moment (Figure 1b), but brings with it the

challenges of 3D nanofabrication. Fabrication of the upright SRR has been realized on the millimeter scale [12], micrometer scale [13], and nanoscale [14], [15]. We accomplish the fabrication of our structure through using a double patterning step of electron beam lithography.

Figure 1

The 3D SRR breaks the 2D symmetry often assumed with planar plasmonic structures. The use of “plasmon tomography” demonstrates the potential of mapping SPR modes in three dimensions [8], [16]–[19], something which is particularly relevant with complex 3D nanostructures where the structure itself does not possess planar symmetry. Previous studies have shown that even planar structures have broken symmetry along the normal direction because of the presence of a substrate, which causes a slight energy shift in modes adjacent to the substrate [17]. Studies on other 3D structures have reconstructed the 3D eigenmodes of the shape [18] and the 3D electric fields of individual plasmon modes [19]. We believe that with the 3D nature of the upright SRR in our study, plasmon tomography may reveal unique and interesting insights into the vectorial nature of the different modes and the localization of plasmonic fields. The use of cathodoluminescence (CL) plasmon tomography has very strict sample requirements, since the large CL mirror prevents tilting of the stage, and would not be possible with our fabricated sample. In our work, we study the 2D projection of the SPR modes with two complementary techniques: electron energy loss spectroscopy (EELS) and cathodoluminescence spectroscopy (CL).

Surface plasmons can be probed with either the use of photon-based techniques or fast electron

based techniques. The use of fast electron based techniques, namely EELS and CL, provides detailed spatial mapping of the field intensity of SPR modes [20]–[24]. In EELS, SPR modes are visible in the low-loss region of the spectrum, typically within the first few electron volts of energy loss. We use a monochromated electron beam and post-processing deconvolution techniques [25] to resolve low-energy SPR signals down to the mid-infrared energy range. While EELS probes the excitation of SPR modes, CL collects the light emitted from the decay of SPR modes into far-field radiation and is thus limited to the detection of radiative modes [26].

Characterization of the SPR modes of the planar SRR has been carried out in great detail with EELS [10], including tilting the SRR to different angles under the beam [8]. To date, studies of the upright SRR have been done with photon-based methods on large scale metamaterial structures [12], [15], but to the best of our knowledge electron-based spectroscopies have not been used to study an upright SRR. We fabricate the upright SRR and perform both EELS and CL on the same sample to study the SPR modes present. Examining the EELS data, we find a strong magnetic dipole mode in the near-IR, as described in the Discussion section, but the scattering of the electron beam within the sample is strong and the signal of the higher order SPR modes is weak. From the EELS data alone, we cannot positively identify the nature of the higher order SPR modes. Instead, we turn to the CL data in this energy range to identify three major modes and the spatial locations of the mode intensities. Using this information, we further examine the EELS data in the visible regime and through subtracting neighbouring modes we are able to discover more subtle structure in the higher order modes in the EELS data as well. Our work shows that both EELS and CL can be used in complement to increase the information gained from either technique alone. With a growing interest in producing layered or three-

dimensional plasmonic nanostructures, EELS faces challenges as a transmission technique through thick samples, but can be used effectively to probe lower order SPR modes, which tend to have larger evanescent fields detectable with an aloof electron beam. CL spectroscopy then fills the gap as a probe of higher order SPR modes in the visible regime, with strong collection efficiency irrespective of the thickness of the sample.

Methods

Simulations

We simulate EELS and CL experiments with the use of the Metallic Nanoparticle Boundary Element Method (MNPBEM) toolbox in Matlab [27]. The MNPBEM toolbox uses the boundary element method [28] to solve Maxwell's equations on the surface of the nanoparticle. The mesh for the SRR was defined using Blender 3D modelling software [29]. To calculate the CL scattering cross-section, we integrate the far field intensity around the structure. We calculate the spectra by simulating an electron beam positioned at a given point and extracting either the EEL probability or the CL scattering cross-section as a function of energy, using the full retarded calculation available in MNPBEM. The maps are obtained by calculating the EEL probability or scattering cross-section for a given energy in a grid across one quarter of the structure, taking advantage of the mirror symmetries present to reduce the computational time required. We use the MNPBEM eigenmode solver, in the quasistatic approximation, to calculate the eigenmodes of the upright SRR and an SRR with different symmetry on the rims to explore how fabrication defects could affect the eigenmodes.

Fabrication

Electron beam lithography (EBL) is a technique frequently used to fabricate custom nanostructures on a variety of substrates. We use EBL to fabricate the upright SRRs on a TEM grid with 50 nm thick silicon nitride windows [30]. In the first fabrication step, we spincoat a layer of electron beam resist, 950 kg/mol poly(methyl methacrylate) (PMMA), onto the TEM grid at a speed of 6000 RPM for 90 seconds, followed by baking at 175°C for five minutes. We then use a JEOL 7000F SEM equipped with Nanometer Pattern Generation System (NPGS) software to expose the resist. We develop the sample in a solution of 1:3 methyl isobutyl ketone (MIBK):isopropanol (IPA) for 120 seconds, followed by rinsing with isopropanol. We coat the developed grid with 2 nm of chromium as an adhesion layer and 30 nm of gold using electron beam evaporation, before lift-off of the remaining electron beam resist in acetone.

To fabricate the three-dimensional structure, we must repeat the EBL process with precise alignment to the first deposition. We spincoat a layer of 495 kg/mol PMMA, followed by two layers of 950 kg/mol PMMA at the same conditions as used in the first step, following each spincoat step with a five minute bake at 175°C. In the SEM, we align to sacrificial alignment marks deposited in the first step and expose the fresh electron beam resist. Once again, we develop in MIBK:IPA for 120 seconds and deposit 70 nm of gold before lift-off in acetone.

As a result of the differences in fabrication between the horizontal and upright SRRs, the details of the SRR are different: the horizontal SRR (modelled in Figure 1a) is a solid planar structure; the upright SRR (modelled in Figure 1b) is not merely the same structure rotated by 90 degrees, but has hollow vertical pillars. During coating of the second gold layer, gold coats the sidewalls of the thicker photoresist and creates the hollow pillars.

Electron energy loss spectroscopy

We use a monochromated FEI Titan 80-300 (“low-base” configuration) scanning transmission electron microscope (STEM) microscope, operating at 80 kV with a beam current of approximately 50 pA, to acquire EEL spectrum images with an energy resolution of approximately 60 meV. EEL spectra are acquired with a dispersion of 5 meV per channel on a Gatan Tridiem (model 865) spectrometer. We apply the Richardson-Lucy algorithm [25], [31] to reduce the broadening effect of the system point spread function and increase the effective energy resolution to 40 meV. With this, we are easily able to resolve the lowest order peaks present in the SRR structure. In addition, due to the high noise present in the EEL signal transmitted through the structure itself, we perform a threshold on the spectrum images before deconvolution to filter out low signal pixels. The acquisition time used for each spectrum is 1 millisecond, in addition to the read-out time of the spectrometer.

Cathodoluminescence

After acquiring the EELS data in the STEM, we collect the cathodoluminescence data on the same sample using an FEI XL-30 field emission SEM, operated at 30 kV with a beam current of 7.5 nA, equipped with a CL mirror and spectrometer (commercial version available from Delmic BV). The system has an acceptance angle of 1.46π and a numerical aperture of 0.95. We are able to acquire a CL spectrum image on the same sample studied with EELS for a direct comparison of the surface plasmon modes. CL data was processed by subtracting a reference spectrum taken from an area of the substrate and correcting for the system response over the spectral region of interest. Use of SEM-CL allows a high collection efficiency and free-space coupling out of the

microscope chamber, with the possibility of inserting polarization filters or imaging cameras. Even so, emission from plasmon decay is low and to optimize the signal to noise ratio (SNR), we use a 1 second acquisition time for each CL spectrum with a dispersion of about 0.85 nm per channel.

Data processing

We use custom code [32] written in the Python programming language to analyze the spectrum images acquired with both techniques. We extract and average spectra from selected pixels within the 3D spectrum image or extract maps of the plasmon resonance modes by plotting the intensity at each pixel summed over a given spectral range. Subtraction of EELS resonance maps was done by first rescaling the intensity of each map between 0 and 1, and then doing a simple pixel-by-pixel subtraction.

Results

The lowest energy mode which appears in the MNPBEM simulations is the strongest mode in both EELS and CL. This mode has a strong peak at 1.035 eV, around the outer edges of the pillars, with no signal between the pillars in the center (Figure 2).

Figure 2

There follows a cluster of high order mode peaks starting after 1.9 eV and extending to around 2.4 eV, corresponding to the visible regime of the spectrum from 650 nm to 500 nm. These

modes are stronger in EELS than they are in CL relative to the intensity of the lowest energy mode. We select the four main peaks, at 1.905, 2.038, 2.384, and 2.446 eV, in this region and display the simulated maps in Figure 2c. To help us identify the nature of the different modes present, we also plot the surface charge density at each peak for a given position of the electron beam (Figure 3b-g). We note that these peaks are closely spaced in energy and overlap with each other, making it difficult to distinguish all of the modes which might be present.

The eigenmode calculation reveals the different plasmon modes which the upright SRR (Figure 4a) supports. We plot the first six eigenmodes in Figure 4, showing two classic SRR modes (Figure 4b, g) and four coupled dipole modes concentrated on the rims of the pillars (Figure 4c-f). Further eigenmodes consist of higher order SRR modes and coupled quadrupole and higher order rim modes (not shown). We also plot the eigenmodes of an upright SRR in which we have broken the symmetry of the pillar rims by making the inner part of the rims shorter as shown in Figure 4h. This was done to explore the potential effects of fabrication defects on the structure of the eigenmodes. In the SRR with broken symmetry, we observe the same primary SRR mode followed by four coupled dipole rim modes and a mode which appears to be a mix of a quadrupole rim mode and the second order SRR mode. The eigenmodes were calculated using the quasistatic method, while the rest of the simulations were performed taking retardation effects into account; because retardation effects are important in a structure of this size, we cannot directly compare the calculated eigenenergies with the results of the simulated spectra. Nevertheless, we can use the surface charge eigenmodes as meaningful descriptors of the resonances supported by this SRR, as in the work by Collins *et al.* [18].

Figure 3

The experimental EELS results (Figure 5a-d) show a strong SPR mode around 0.6875 eV, followed by a broad collection of modes between 1 eV and 2.5 eV (495 nm to 1240 nm). There is very little EELS signal from electrons passing through the structure itself, making it necessary to filter out low-signal pixels to reduce the noise in the normalized and deconvolved data. By selecting different areas around the structure (Figure 5i), we are able to locate individual peaks in the spectrum corresponding to higher order SPR modes. We obtain the plasmon intensity maps by filtering the spectrum image within a range of energies, as shown in Figure 5b-d.

Figure 4

CL results are obtained in the visible region of the electromagnetic spectrum only, scanning a range from about 1.25 eV to 3 eV. There are three dominant SPR peaks in CL at around 1.37 eV, 1.72 eV, and 2.12 eV (Figure 5i). Filtering the spectrum image around these peaks reveals that there is significant structure in the intensity of the SPR modes around the outer edges of the 3D pillars (Figure 5f-h). There is some asymmetry present in each of the intensity maps, both between the left and right pillars and in the emission from the top to the bottom.

Figure 5

Discussion

Plasmon Mode Identification

Before we can begin to identify the different modes present in the sample, we must address the differences in energy between the peaks present in simulation and those present in the experimental data. The mode energies of the simulations (Figure 2), when compared to experiment (Figure 5), are blue-shifted. We attribute this to the presence of the substrate in the experiments [33], which was not taken into account during simulation, and to differences in the simulated structure compared to the fabricated structure. The presence of the substrate causes additional damping of the SPR modes and changes the dielectric environment of the mode, thereby changing its energy. The dimensions of the structure may be slightly different between simulations and experiment and there will be small defects in the fabricated structure which will particularly affect the higher order modes. In particular, it seems that the pillars are closer together in the fabricated SRR compared to the simulation, which will result in a stronger coupling between the pillars and would make the differences between the different modes more evident in the surface charge maps. We also expect that there will be some imperfections in the shape of the pillars which could affect the energies of the rim modes.

The change in energy between the EELS and CL peaks has been observed in previous studies, for instance in the work of Losquin and Kociak [34] and is correlated with the damping of surface plasmon modes [35] and differences between the full (EELS) and the radiative electromagnetic density of states (CL) [21], [34]. We also note that changes in the SPR peak locations could result from changes to the dielectric environment because of the multiple acquisitions in the TEM and subsequently in the SEM, during which the electron beam may cause the deposition of a layer of carbon over the structure leading to additional and possibly significant shifts in the CL peaks.

Considering the lowest energy mode found, we identify a strong mode in EELS at 0.69 eV (Figure 5b), too far into the infrared for the CL system to detect. This mode has a broad evanescent field which matches with that seen in the simulation data at 1.035 eV. Calculating the magnetic field lines (Figure 3a) reveals that this mode is the magnetic dipole mode expected in a typical split ring resonator [10]; notable in our structure for its direction within the plane of the sample and perpendicular to the incident electron beam.

In analyzing the higher order SPR modes, we are now within the spectral range of the CL spectrometer and can take full advantage of the information contained therein. Before we begin to classify the modes we find, we must address the asymmetries found in the CL maps. The asymmetry in the first two CL maps (Figure 5f,g) may be at least partially attributed to the asymmetries present in the structure as-fabricated; compared to the ideal SRR, the fabricated structure contains some defects which may strongly affect the emission and strength of the higher order modes. The higher order modes have short effective SPR wavelengths and so can be more greatly affected by small defects in the fabricated structure. For instance, the height of the pillar may not be exactly equal all around the circumference, affecting the electron beam interaction probability and the strength of the emission at different locations around the pillar. We note that all the plasmon maps, in both EELS and CL, show greater intensity on the left pillar (Figure 5b-d, f-h), which we attribute to a smoother and more refined shape of the left pillar compared to the right.

The asymmetry from the top to the bottom of the SRR may come from the collection parameters of the CL system. The mirror in the CL system collects light from only a finite solid angle of

emission; in our case, the parabolic mirror is located towards the top of the image and will only collect light emitted in that direction. Light emitted towards the bottom of the image or underneath the sample will not be collected at all. Because of the 3D nature of our structure, we would expect that the emission of light normal to the structure is not symmetrical around the sample plane. Using the EELS and CL data and comparing with the results of our calculations, we can begin to identify the high order modes present in the SRR structure.

We do not see, in the upright SRR, exactly the same set of eigenmodes as expected for a planar SRR [10], [36]. The classic SRR resonances are present as eigenmodes (Figure 4b,g,i) , but are comparatively weaker and are not seen in experiment. As the orientation of the electron beam relative to the SRR changes, the excitation probability for these modes changes [8] and we expect that these classic SRR resonances have a very small excitation probability when the SRR is in this upright orientation. We observe in our experimental data and simulations that the 3D shape gives the opportunity for a different set of modes to dominate the collected signal, as we shall discuss next. Examining the hollow structure of the pillars on the upright SRR, we can consider the modes in the pillars (Figure 4c-f,j-m) as arising from the coupling of dipole modes around the rims of the pillars.

In a single rim, the lowest order mode will be the dipole mode and will appear at the same energy for all polarizations across the rim; when another rim is brought into proximity with the first, this dipole mode splits into longitudinal and transverse bonding and anti-bonding modes found at different energies [37], as can be seen in the plasmon eigenmode expansion (Figure 4c-f). Changing the symmetry of the coupled rims (Figure 4h) will change the order of the rim

eigenmodes. With the 'perfect' structure (Figure 4a), we observe that the longitudinal bonding mode is at the lowest energy, followed by the transverse bonding and anti-bonding modes, then the longitudinal anti-bonding mode. With a relatively small change in symmetry (Figure 4h), the longitudinal bonding and anti-bonding modes appear first, followed by the transverse bonding and anti-bonding modes, because of the small change in the shape of the pillars. This suggests that the order of the coupled rim modes may depend strongly on the fabrication quality and exact geometry.

In the lowest energy mode visible in CL, at 1.375 eV (Figure 5f), we observe higher intensity in the gap between the pillars, allowing us to match it with the second mode seen in simulations, at 1.905 eV (Figure 2c). Comparing this with the surface charge distribution (Figure 3c), we classify this mode as the longitudinal bonding mode of the coupled rim modes on the pillars. Expecting that the spatial distribution of this mode would be the same in the EELS data, it would be very difficult to retrieve any signal because of the high scattering of the electron beam within the structure, where the mode intensity should be highest. We also observe that, in the simulated spectrum, the longitudinal bonding mode is, at most, a shoulder on the peak of other rim modes (Figure 2b) and therefore we conclude that this mode has very weak coupling to the electron beam. We suggest, however, that because the mode has a strong dipole moment, it may couple strongly to radiation, providing a strong CL signal despite a weak EELS signal.

The longitudinal anti-bonding mode occurs at 2.038 eV in the simulations (Figure 2c), with the calculated surface charges shown in Figure 3f. We would expect the map from this mode to show more intensity towards the outer edges of the pillars, as we see in the experimental CL peak at

1.725 eV (Figure 5g). With the overlapping of tails from the peak at 1.375 eV, we still note some intensity towards the center of the structure in the CL data, but the intensity distribution of this mode can be made very clear by observing the difference map (Figure 6a). The longitudinal anti-bonding mode might be expected to be non-radiative, however, we see it clearly in both the CL data and simulation. The large size of the SRR compared to the wavelength of light means that retardation effects will contribute significantly to the SPR modes seen; non-dipole modes may be radiative when retardation effects play a role [38], [39]. In addition to this, we suggest that the conductive coupling of the pillars through the rest of the SRR structure changes the charge configuration of the anti-bonding rim mode (Figure 3f) enough to produce a net dipole configuration and allow the anti-bonding mode to radiate. This is further aided in the experimental structure by asymmetries from the fabrication of the SRR, which can cause modes which would typically be considered dark to radiate [40].

In the EELS data, we observe two peaks in addition to the first order magnetic dipole mode: at 1.420 eV (Figure 5c) and 1.772 eV (Figure 5d). These two peaks are at high energies and their fields are more tightly confined to the SRR than the magnetic dipole peak at 0.6875 eV. Combined with the noise in the spectrum, the tight confinement makes it difficult to distinguish the differences between the two peaks and identify the type of mode to which each corresponds. To make it easier to see the structure associated with each peak, we take difference maps between neighbouring peaks (Figure 6c).

The low energy peak, at 1.420 eV, has a high intensity towards the left outer edge of the SRR (blue in Figure 6c), implying that this mode is a longitudinal mode. It is difficult to distinguish

between the bonding and anti-bonding longitudinal modes based on the EELS data alone, because of the high scattering of the electron beam within the structure, where the intensity for the bonding mode should be high. The high intensity at the outer edges of the pillars suggests that this mode is most likely to be the longitudinal anti-bonding mode, implying that the longitudinal bonding mode is not visible in our EELS data at all, because of a combination of the scattering of the electron beam and the low excitation probability, as seen in the simulated spectra (Figure 2b).

The highest energy EELS peak, at 1.772 eV, is difficult to identify without the difference maps. In comparison to the 1.420 eV peak, the 1.772 eV peak has more intensity around the sides of the pillars, suggesting it might be a transverse rim mode.

To more easily compare the EELS and CL data, we also create difference maps between neighbouring CL modes (Figure 6a, b). The CL difference map between the 1.725 eV and 1.375 eV peaks, in Figure 6a, has been discussed above. The other CL difference map (Figure 6b), between the peaks at 2.120 eV and 1.725 eV, shows that the higher energy peak has strong intensity at the sides of the pillars, while the lower energy peak has a high intensity at the left outer edge of the SRR. Masking the pixels which correspond to the location of the sample (where the scattering is strong and recorded EELS intensity is very low) allows us to visually compare this difference map with the EELS difference map between 1.772 eV and 1.420 eV. The two difference maps, from CL and EELS, compare very well. The comparison supports the argument that the 1.772 eV EELS peak is the same as the 2.120 eV CL peak and that the 1.420 eV EELS peak is the same as the 1.725 eV CL peak, despite the differences in energy between the two techniques, which may arise from the differences between the full and the radiative

electromagnetic density of states, damping in the substrate, or the build-up of carbon contamination under the electron beam in the SEM vacuum chamber.

Figure 6

The highest energy SPR mode of the three that we observe in CL (2.120 eV, Figure 5h) and EELS (1.772 eV, Figure 5d) can be immediately identified as a transverse rim mode because of its high intensity towards the sides of the pillars. The transverse bonding and anti-bonding modes show clearly in the eigenmode calculation (Figure 4d,e), but do not have clearly separated peaks in the spectrum (Figure 2b). By placing the simulated electron beam towards the sides of the pillars, we can see that the transverse mode response is mixed with that of the nearby longitudinal mode responses (Figure 3d,e). The surface charge distribution in Figure 3d, at 1.905 eV, hints that the transverse bonding mode is near this energy, but perhaps dominated by the longitudinal bonding mode. At 2.038 eV, the peak we identified as the longitudinal anti-bonding mode, placing the electron beam at the side of the pillar (Figure 3e) induces surface charges similar to the transverse anti-bonding eigenmode in Figure 4f. Although in the simulation of the ideal structure, the transverse modes are in between the two longitudinal rim modes, we would like to emphasize that small changes in the symmetry can cause changes in the order in which the eigenmodes will appear (Figure 4j-m). Without the use of tomography and quantitative measurements of the precise and exact dimensions on such a complex 3D structure, it is difficult to know exactly what the shape of each rim is. Due to this sensitivity, we can only suggest that the symmetry of the rims is broken in such a way to favour the transverse rim modes being at a higher energy than the longitudinal rim modes.

In general, the spatial distributions of the transverse bonding and anti-bonding rim modes will appear identical in EELS data and be very difficult to differentiate except by energy and prior knowledge of the mode order, since EEL measurements are not sensitive to the plasmon phase. However, based on the symmetries of the charge configuration, we might expect that the transverse bonding mode will be non-radiative and distinguishable from the transverse anti-bonding mode based on correlative EELS and CL. With retardation effects and the asymmetries present in our structure which may change the radiative properties of the modes, it is difficult to discern differences between these two modes, and we can only identify the mode at 2.120 eV in CL and 1.772 eV in EELS as a transverse rim mode.

The mode at 2.384 eV (Figure 3g) in the simulations appears to be a fourth order mode which might be found in a classic SRR [10]. We expect that this mode, and other classic SRR modes, may have a weak coupling to the electron beam because of the orientation of the SRR. It may be present in the spectrum, but very weak or at a high enough energy that it cannot be distinguished from the bulk plasmon, as we observe that it is also very close to the bulk plasmon in the simulated spectrum.

In the simulations, we also observe EEL signal arising around 2.4-2.5 eV, which we attribute to the bulk plasmon of gold. There is very little signal in the CL spectra (Figure 2b) at these energies (simulated maps are normalized individually): any transitions in this range are non-radiative. In the CL maps we begin to see that the edges of the structure develop a very narrow feature at high energies (2.384, 2.446 eV), where the CL signal is low and the normalization of

the maps emphasizes very minor differences in signal. It is likely that this is appearing as a result of the numerical treatment of the SRR mesh and simulated electron beam. We note that the fine variations along this feature correspond well to the nodes used in the simulation mesh. The EEL map at 2.446 eV becomes brighter where the thickness of the gold is higher, corresponding to a longer transit time of the electron beam through the gold. We do not see the bulk plasmon in the experimental EELS data because of the high scattering and lack of signal from the electron beam passing through the structure.

Correlative Spectroscopy of 3D Structures

Each technique we have used brings its own unique advantages to the study of SPR modes; we show the value of using both techniques in conjunction when facing the challenge of analyzing a three-dimensional structure. EELS covers a broad energy range and reveals the whole spectrum of resonance modes in a single spectrum image acquisition. EELS makes it possible to detect both bright and dark modes, but plasmon peak extraction suffers from proximity to the zero loss peak, with the peaks of interest lying on the broad tail of the zero loss peak intensity. When studying a 3D nanostructure, EELS reveals an additional weakness as a transmission technique: the thick gold structure causes high scattering of the electron beam, resulting in low signal reaching the EEL spectrometer. EELS cannot detect the fine spatial structure of the SPR modes within the 3D sample itself because of this scattering and we can obtain information on the modes only from aloof excitation of SPR.

The SPR fields we are able to detect in EELS come from a combination of inelastic delocalization of low energy loss processes and the extent of the evanescent field of the SPR

itself. Delocalization in the low loss regime of the EEL spectrum can restrict the achievable spatial resolution [41], making low energy plasmon modes appear broader spatially than predicted [42]. The spatial broadening of the lowest energy modes also comes from the sloping background of the zero loss peak; this effect is reduced after RL deconvolution is applied [25]. These delocalization factors prove to be helpful in detecting SPR modes in 3D structures, in which most of the signal is scattered by the thick specimen, by increasing the signal obtained using an aloof beam configuration.

The lowest energy modes, such as the magnetic dipole mode in the SRR, will have the largest plasmon wavelength, which, in combination with the dielectric functions of the metallic structure and the medium it is present in, affect the SPR field confinement [43]. Regardless of the thickness of the sample, the electron beam will be able to interact with at least the lowest energy modes outside the structure. Higher energy modes will tend to be more tightly confined to the metal and will be harder to detect in highly scattering samples: the electron beam must be very close to or on top of the structure to interact with the SPR field and excite a resonance. This implies that for EELS on thick or highly scattering samples, the tightly confined modes will be very difficult to probe due to poor SNR over the top of the structure. With lighter elements or the more common 2D thin film samples, scattering of the electron beam is less of a problem and with sufficient current, tightly confined modes and cavity modes are accessible with EELS.

Comparing the spatial resolution of STEM-EELS and SEM-CL, due to the difference in probe size between the two instruments and the operation at different accelerating voltages (80 kV in the STEM and 30 kV in the SEM), we are able to obtain a much higher resolution with STEM

data than what is achievable with SEM-CL (compare Figure 5a and 5f). We suggest that the high spatial resolution of STEM-EELS could be used to determine if there are fine details in the SPR mode structure which cannot be resolved in the SEM-CL data. With the modes we are studying, it does not appear that the SPR features are smaller than the SEM-CL spatial resolution can identify.

The CL signal collected does not rely, as EELS does, on the detection of evanescent fields through aloof excitation. We have shown in our analysis of the plasmon modes how the CL signal can be used to provide missing information on the mode structure of the tightly confined higher order modes, allowing us to identify the character of the resonance modes, although it does not cover the same spectral range as EELS. Interestingly, we have found that the longitudinal bonding mode has very weak signal in EELS, but strong signal in CL, both in simulation and experiment. This is likely due to the configuration of the SPR electric fields; with a strong net dipole moment, it could be expected to have strong radiative properties, but because of the orientation of this dipole moment, the components of the field parallel to the electron beam are weak, and so coupling to the electron beam is weak.

An interesting point to note for the study of a 3D structure is in the theoretical link between the EEL signal and the electromagnetic local density of states, as established by Kociak and Garcia de Abajo [44]. Included in the derivation is invariance of the sample along the z-direction, or beam propagation direction: the structure is assumed to be planar. Building the 3D structure, as we have done here, breaks the symmetry along this direction and the assumption of z-invariance no longer holds, which may have some interesting implications for the given relationship

between EEL signal and the LDOS of the structure: the relationship is unlikely to be as simple as in the 2D case.

Finally, from a practical point of view regarding the collection parameters, we must acquire for a much longer time and much higher beam current to collect enough CL signal compared to EELS, bringing additional problems related to sample drift and contamination build-up. CL signal relies on both excitation and emission probabilities, while the EEL signal requires only excitation. We do gain benefits in CL from the necessity of fabricating the sample on an electron-transparent substrate for EELS analysis. With a thin membrane supporting the SRR, there is very little background CL signal coming from interactions of the electron beam with the substrate, something which can be a significant source of unwanted signal, but we may experience shifts in the plasmon energy because of the collection of carbon contamination and change in the dielectric environment under the electron beam in the relatively poor vacuum of the SEM.

Concluding Remarks

We have fabricated a single upright nanoscale split ring resonator and studied its plasmon resonance modes using both electron energy loss spectroscopy in a STEM and cathodoluminescence in an SEM, complemented with simulations of the plasmonic response under electron beam excitation. We find that the use of both experimental techniques offers more insight into the resonance modes than either technique would if used alone. From the EELS data, we identify the magnetic dipole moment classic to the SRR, at 0.69 eV energy loss. Using the CL data, we identify the higher order modes in the visible regime of the electromagnetic spectrum, and denote these as longitudinal bonding and anti-bonding rim modes around the rims of the

hollow pillars, and a transverse mode arising from coupling of rim modes on the upright SRR. We further examine the EELS data by using difference maps between modes close in energy to reveal the finer structure of the mode intensity. We confirm our mode assignment with calculated spectra, intensity maps, and surface charge density distributions using the MNPBEM software.

We provide a comparison of EELS and CL and show how each of them can compensate for deficiencies of the other to provide more complete information on a three-dimensional sample. The high scattering of the transmitted electron beam inside the 3D sample is a difficult limitation to overcome for EELS, but not for CL, where a good SNR for SPR radiation can be obtained over the whole structure independent of thickness. The CL signal, however, is limited to radiative modes emitting within the spectral range covered by the chosen optical spectrometer, whereas EELS can cover the full spectral range of interest and probes both dark and bright plasmon modes. The two techniques can be performed on exactly the same nanostructure, as we have shown here, provided the compatibility with TEM is ensured, giving a direct correlation between the signals obtained from each. Finally, the results presented here highlight the need to use both EELS and CL to study three-dimensional nanostructures to provide a more complete understanding of the SPR modes present.

Funding

This work was supported by the Natural Sciences and Engineering Research Council of Canada (NSERC) under the Discovery Grant Program (ICB, EPB, GAB); The Netherlands Organization for Scientific Research (SM, AP); and the European Research Council (ICB, SM, AP) [695343 – SCEON].

Acknowledgements

The EELS work was carried out at the Canadian Center for Electron Microscopy, a national facility supported by The Canadian Foundation for Innovation under the MSI program, NSERC, and McMaster University. The CL work at AMOLF is part of the research program of The Netherlands Organization for Scientific Research (NWO); it is also funded by the European Research Council. S.M. and I.C.B. acknowledge Dr. Toon Coenen from Delmic BV for useful discussion and advice regarding CL analysis. ICB is also grateful to the Faculty of Engineering at McMaster University for the Dean's Excellence Award; NSERC funding under the Alexander Graham Bell Canada Graduate Scholarship program; and travel funding from the NSERC Michael Smith Foreign Study Supplement.

Competing financial interest: A.P. is co-founder and co-owner of Delmic BV, a company that has brought a cathodoluminescence system on the market based on a design developed at AMOLF and used in this work.

References

[1] Zheludev NI (2010) The Road Ahead for Metamaterials. *Science* **328**, 582–583.

[2] Smith DR, Pendry JB, and Wiltshire MCK (2004) Metamaterials and negative refractive index. *Science* **305**, 788-792.

[3] Pendry JB, Holden AJ, Robbins DJ, and Stewart WJ (1999) Magnetism from conductors and enhanced nonlinear phenomena. *IEEE Trans. Microw. Theory Tech.* **47**, 2075–2084.

[4] Smith DR, Padilla WJ, Vier DC, Nemat-Nasser SC, and Schultz S (2000) Composite Medium with Simultaneously Negative Permeability and Permittivity. *Phys. Rev. Lett.* **84**,

4184–4187.

[5] Gay-Balmaz P, and Martin OJF (2002) Electromagnetic resonances in individual and coupled split-ring resonators. *J. Appl. Phys.* **92**, 2929–2936.

[6] Ding C, Jiang L, Sun C, Wu L, Xu D, Zhang G, and Yao J (2015) Stable terahertz toroidal dipolar resonance in a planar metamaterial. *Phys. Status Solidi B* **252**, 1388–1393.

[7] Katsarakis N, Konstantinidis G, Kostopoulos A, Penciu RS, Gundogdu TF, Kafesaki M, Economou EN, Koschny Th, and Soukoulis CM (2005) Magnetic response of split-ring resonators in the far-infrared frequency regime. *Opt. Lett.* **30**, 1348–1350.

[8] von Cube F, Niegemann J, Irsen S, Bell DC, and Linden S (2014) Angular-resolved electron energy loss spectroscopy on a split-ring resonator. *Phys. Rev. B* **89**, 115434.

[9] Hancu IM, Curto AG, Castro-López M, Kuttge M, and van Hulst NF (2014) Multipolar Interference for Directed Light Emission. *Nano Lett.* **14**, 166–171.

[10] Boudarham G, Feth N, Myroshnychenko V, Linden S, García de Abajo J, Wegener M, Kociak M (2010) Spectral Imaging of Individual Split-Ring Resonators. *Phys. Rev. Lett.* **105**, 255501.

[11] Linden S, Enkrich C, Wegener M, Zhou J, Koschny T, and Soukoulis CM (2004) Magnetic Response of Metamaterials at 100 Terahertz. *Science* **306**, 1351–1353.

[12] Han S, Cong L, Lin H, Xiao B, Yang H, and Singh R (2016) Tunable electromagnetically induced transparency in coupled three-dimensional split-ring-resonator metamaterials. *Sci. Rep.* **6**, 20801.

[13] Chen CC, Hsiao CT, Sun S, Yang K-Y, Wu PC, Chen WT, Tang YH, Chau Y-F, Plum E, Guo G-Y, Zheludev NI, and Tsai DP (2012) Fabrication of three dimensional split ring resonators by stress-driven assembly method. *Opt. Express* **20**, 9415–9420.

[14] Liao CY, Chen MK, Huang Y-W, Chen WT, Wu PC, Tsai W-Y, Lin HT, Huang Y-T, Chen T-Y, Chen J-W, Savinov V, Zheludev NI, and Tsai DP (2015) Optical toroidal response in three-dimensional plasmonic metamaterial. *Proc. of SPIE* **9547**, 954724.

[15] Wu PC, Hsu W-L, Chen WT, Huang Y-W, Liao CY, Liu AQ, Zheludev NI, Sun G, and Tsai DP (2015) Plasmon coupling in vertical split-ring resonator metamolecules. *Sci. Rep.* **5**, 9726.

[16] Atre AC, Brenny BJM, Coenen T, García-Etxarri A, Polman A, and Dionne JA (2015) Nanoscale optical tomography with cathodoluminescence spectroscopy. *Nat. Nanotechnol.* **10**, 429–436.

[17] Nicoletti O, de la Peña F, Leary RK, Holland DJ, Ducati C, and Midgley PA (2013) Three-dimensional imaging of localized surface plasmon resonances of metal nanoparticles. *Nature* **502**, 80–84.

[18] Collins SM, Ringe E, Duchamp M, Saghi Z, Dunin-Borkowski RE, and Midgley PA (2015) Eigenmode Tomography of Surface Charge Oscillations of Plasmonic Nanoparticles by Electron Energy Loss Spectroscopy. *ACS Photonics* **2**, 1628–1635.

[19] Hörl A, Haberfehlner G, Trügler A, Schmidt F-P, Hohenester U, and Kothleitner G (2017) Tomographic imaging of the photonic environment of plasmonic nanoparticles. *Nat. Commun.* **8**.

[20] García de Abajo FJ (2010) Optical excitations in electron microscopy. *Rev. Mod. Phys.* **82**, 209–275.

[21] Losquin A, Zagonel LF, Myroshnychenko V, Rodríguez-González B, Tencé M, Scarabelli L, Förstner J, Liz-Marzán LM, García de Abajo FJ, Stéphan O, and Kociak M (2015) Unveiling Nanometer Scale Extinction and Scattering Phenomena through Combined

Electron Energy Loss Spectroscopy and Cathodoluminescence Measurements. *Nano Lett.* **15**, 1229–1237.

[22] Saito H, and Yamamoto N (2015) Control of Light Emission by a Plasmonic Crystal Cavity. *Nano Lett.* **15**, 5764–5769.

[23] Nelayah J, Kociak M, Stéphan O, García de Abajo FJ, Tencé M, Henrard L, Taverna D, Pastoriza-Santos I, Liz-Marzán LM, and Colliex C (2007) Mapping surface plasmons on a single metallic nanoparticle. *Nat. Phys.* **3**, 348–353.

[24] Zhu XL, Ma Y, Zhang JS, Xu J, Wu XF, Zhang Y, Han XB, Fu Q, Liao ZM, Chen L, and Yu DP (2010) Confined Three-Dimensional Plasmon Modes inside a Ring-Shaped Nanocavity on a Silver Film Imaged by Cathodoluminescence Microscopy. *Phys. Rev. Lett.* **105**, 127402.

[25] Bellido EP, Rossouw D, and Botton GA (2014) Toward 10 meV Electron Energy-Loss Spectroscopy Resolution for Plasmonics. *Microsc. Microanal.* **20**, 767–778.

[26] Coenen T, Schoen DT, Mann SA, Rodriguez SRK, Brenny BJM, Polman A, and Brongersma ML (2015) Nanoscale Spatial Coherent Control over the Modal Excitation of a Coupled Plasmonic Resonator System. *Nano Lett.* **15**, 7666–7670.

[27] Hohenester U, and Trügler A (2012) MNPBEM – A Matlab toolbox for the simulation of plasmonic nanoparticles. *Comput. Phys. Commun.* **183**, 370–381.

[28] García de Abajo FJ, and Howie A (2002) Retarded field calculation of electron energy loss in inhomogeneous dielectrics. *Phys. Rev. B* **65**, 115418.

[29] Blender Online Community, *Blender - a 3D modelling and rendering package*. Amsterdam: Blender Foundation. https://www.blender.org/

[30] Koh AL, McComb DW, Maier SA, Low HY, and Yang JKW (2010) Sub-10 nm

patterning of gold nanostructures on silicon-nitride membranes for plasmon mapping with electron energy-loss spectroscopy. *J. Vac. Sci. Technol. B* **28**, C6O45-C6O49.

[31] Gloter A, Douiri A, Tencé M, and Colliex C (2003) Improving energy resolution of EELS spectra: an alternative to the monochromator solution. *Ultramicroscopy* **96**, 385–400.

[32] Bicket IC (2017) *icbicket/DataAnalysis: SpectrumImagingAnalysisPy*, Python program. http://doi.org/10.5281/zenodo.807763

[33] Ringe E, McMahon JM, Sohn K, Cobley C, Xia Y, Huang J, Schatz GC, Marks LD, and Van Duyne RP (2010) Unraveling the Effects of Size, Composition, and Substrate on the Localized Surface Plasmon Resonance Frequencies of Gold and Silver Nanocubes: A Systematic Single-Particle Approach. *J. Phys. Chem. C* **114**, 12511–12516.

[34] Losquin A, and Kociak M (2015) Link between Cathodoluminescence and Electron Energy Loss Spectroscopy and the Radiative and Full Electromagnetic Local Density of States. *ACS Photonics* **2**, 1619–1627.

[35] Zuloaga J, and Nordlander P (2011) On the Energy Shift between Near-Field and Far-Field Peak Intensities in Localized Plasmon Systems. *Nano Lett.* **11**, 1280–1283.

[36] Rockstuhl C, Lederer F, Etrich C, Zentgraf T, Kuhl J, and Giessen H (2006) On the reinterpretation of resonances in split-ring-resonators at normal incidence. *Opt. Express* **14**, 8827–8836.

[37] Tsai C-Y, Lin J-W, Wu C-Y, Lin P-T, Lu T-W, and Lee P-T (2012) Plasmonic Coupling in Gold Nanoring Dimers: Observation of Coupled Bonding Mode. *Nano Lett.* **12**, 1648–1654.

[38] Kottmann JP and Martin OJF (2001) Retardation-induced plasmon resonances in coupled nanoparticles. *Opt. Lett.* **26**, 1096–1098.

[39] Hao F, Larsson EM, Ali TA, Sutherland DS, and Nordlander P (2008) Shedding light on dark plasmons in gold nanorings. *Chem. Phys. Lett.* **458**, 262–266.

[40] Slaughter LS, Wu Y, Willingham BA, Nordlander P, and Link S (2010) Effects of Symmetry Breaking and Conductive Contact on the Plasmon Coupling in Gold Nanorod Dimers. *ACS Nano* **4**, 4657–4666.

[41] Egerton RF (2007) Limits to the spatial, energy and momentum resolution of electron energy-loss spectroscopy. *Ultramicroscopy* **107**, 575–586.

[42] Rossouw D, and Botton GA (2013) Plasmonic Response of Bent Silver Nanowires for Nanophotonic Subwavelength Waveguiding. *Phys. Rev. Lett.* **110**, 066801.

[43] Dionne JA, Sweatlock LA, Atwater HA, and Polman A (2005) Planar metal plasmon waveguides: frequency-dependent dispersion, propagation, localization, and loss beyond the free electron model. *Phys. Rev. B* **72**, 075405.

[44] García de Abajo FJ, and Kociak M (2008) Probing the Photonic Local Density of States with Electron Energy Loss Spectroscopy. *Phys. Rev. Lett.* **100**, 106804.

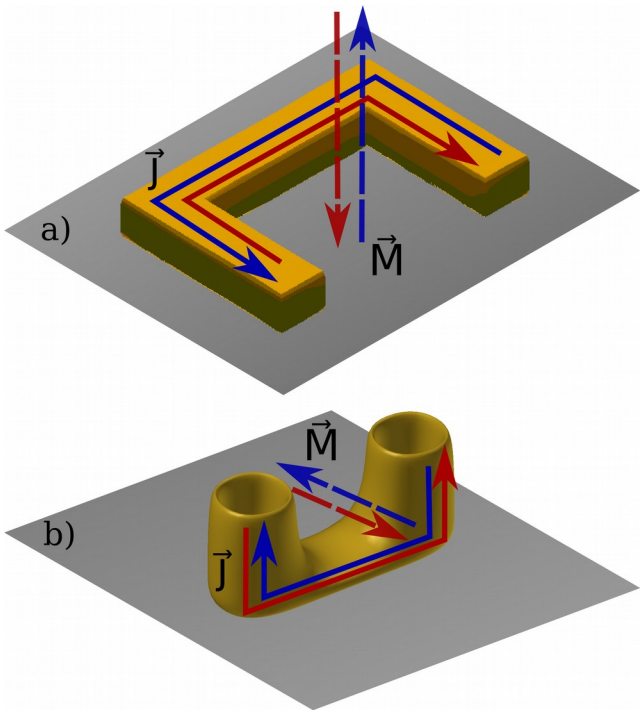

Figure 1: Surface plasmon electrons oscillate around the split ring, represented by current density J, creating a net magnetic dipole moment, M, through the center of the (a) planar and (b) upright split ring resonator.

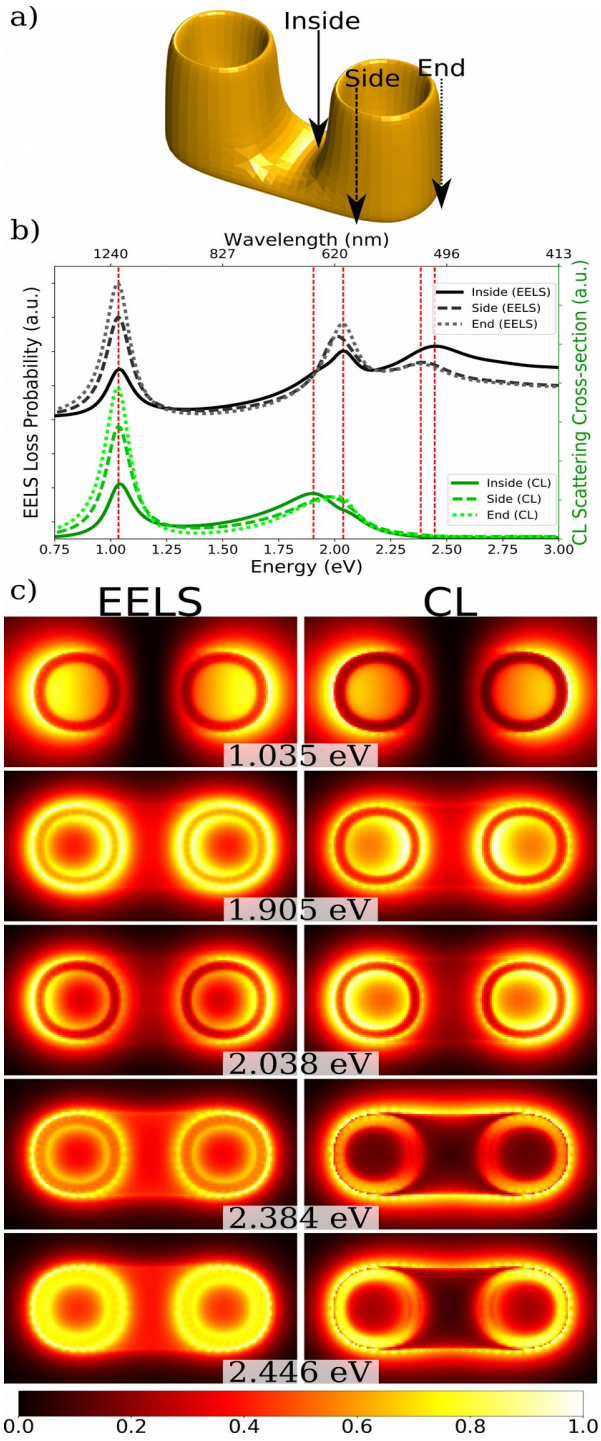

Figure 2: MNPBEM simulations (a) Locations of electron beam excitation for calculated spectra on upright split ring resonator (mesh shown); (b) Calculated EELS loss probability and CL scattering cross-section; (c) Calculated plasmon intensity maps of structure at indicated energies for EELS (left column) and CL (right column).

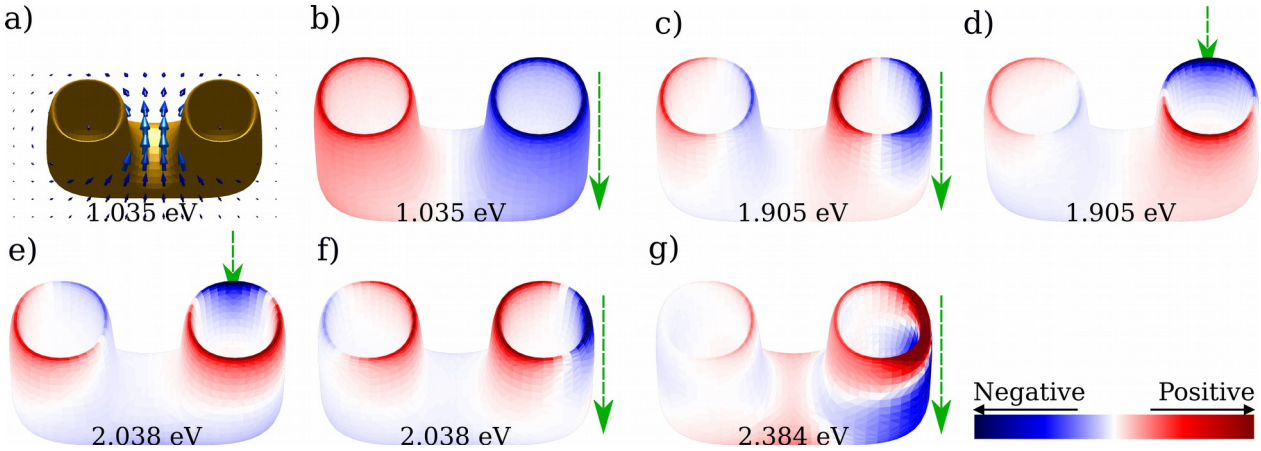

Figure 3: Simulation results for single SRR, green arrow indicates position and direction of electron beam excitation; (a) Magnetic field vectors for SPR mode at 1.035 eV; (b-g) Surface charge density maps for (b) magnetic dipole SPR mode at 1.035 eV; (c) longitudinal bonding rim mode (excited by an electron beam placed at 'End' position, as shown in Figure 2a) mixed with (d) transverse bonding rim mode (excited by an electron beam placed at 'Side' position) at 1.905 eV; (e) transverse anti-bonding rim mode (excited by an electron beam placed at 'Side' position) mixed with (f) longitudinal anti-bonding rim mode (excited by an electron beam placed at 'End' position) at 2.038 eV; (g) fourth order SRR mode at 2.384 eV.

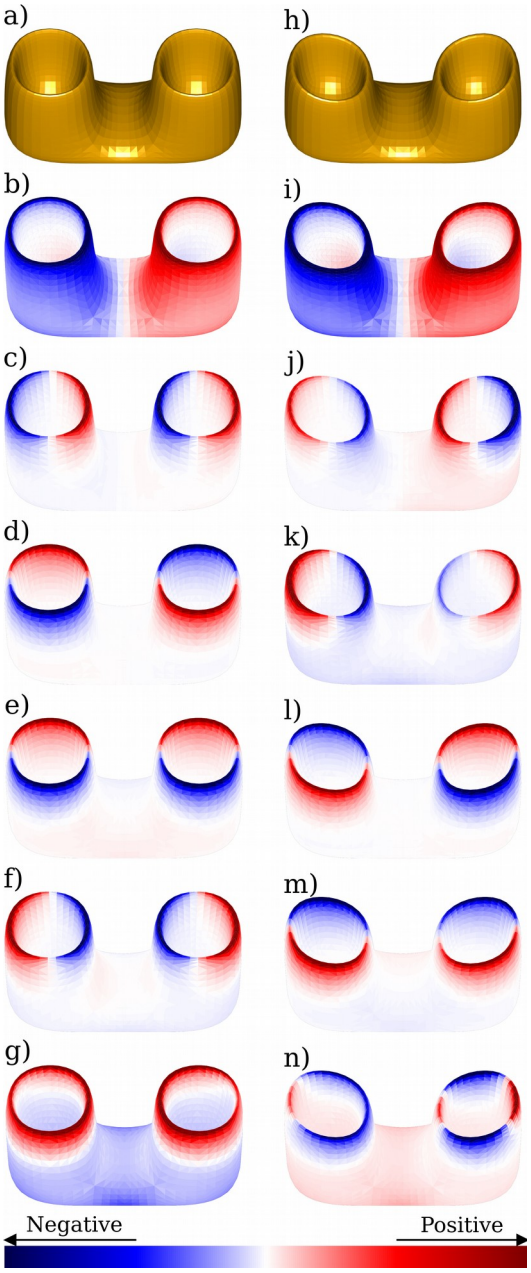

Figure 4: Calculated eigenmodes for an upright SRR (a-g) and an upright SRR with broken symmetry around the rims (h-n). Structure of the upright SRR is shown in (a), followed by the first six calculated eigenmodes in order of increasing energy: (b) SRR dipole mode; (c) Longitudinal bonding rim mode; (d) Transverse bonding rim mode; (e) Transverse anti-bonding rim mode; (f) Longitudinal anti-bonding rim mode; (g) Third order SRR mode. Structure of the upright SRR with broken rim symmetry is shown in (h), followed by the first six calculated eigenmodes in order of increasing energy: (i) SRR dipole mode; (j) Longitudinal bonding rim mode; (k) Longitudinal anti-bonding rim mode; (l) Transverse bonding rim mode; (m) Transverse anti-bonding rim mode; (n) Higher order mode, combination of quadrupole rim modes and third order SRR mode.

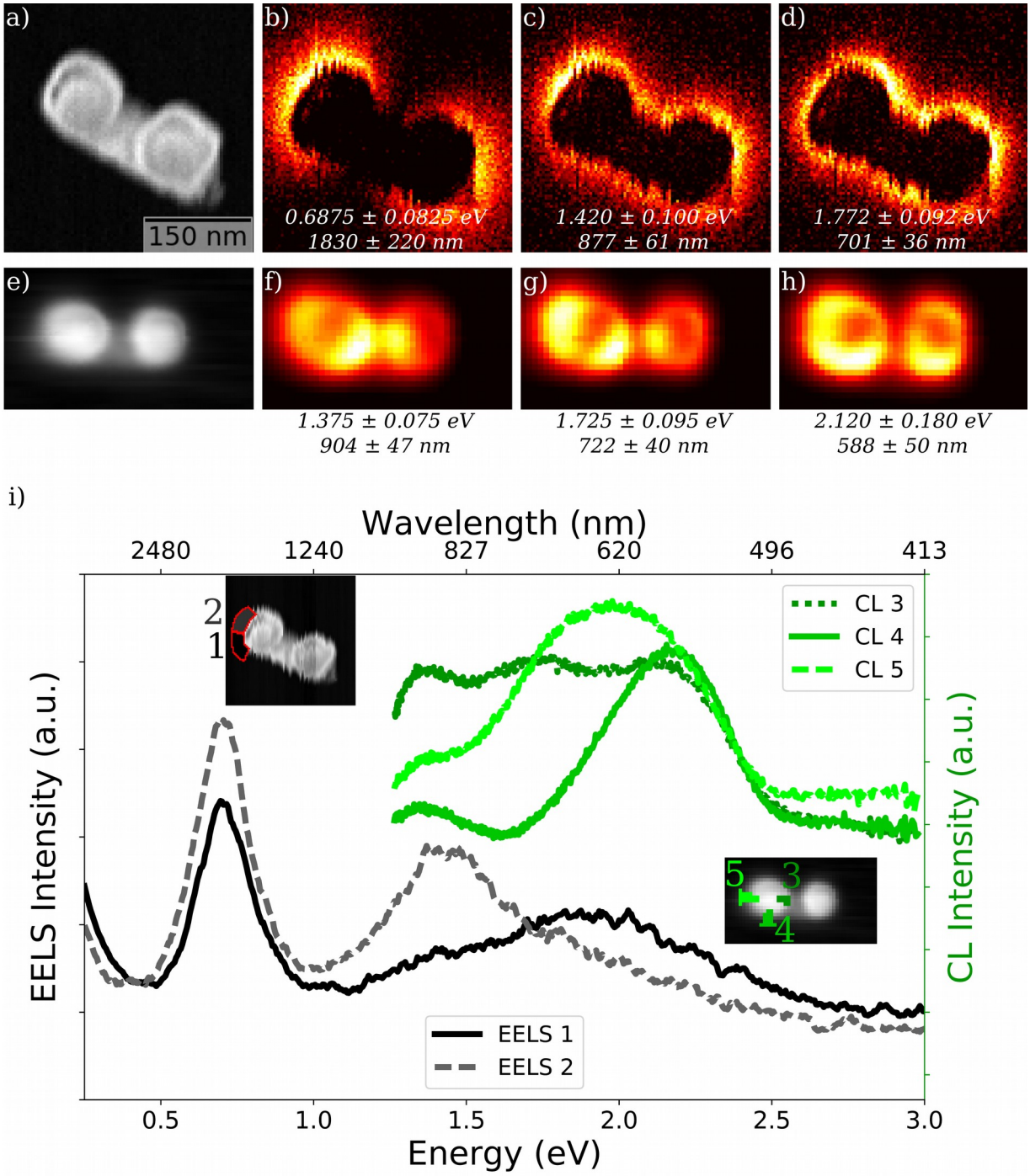

Figure 5: Experimental results from EELS (a-d, i) and CL (e-h, i). (a) High angle annular dark field image of SRR; (b-d) SPR maps extracted from EELS showing (b) the SRR magnetic dipole mode (0.6875 eV); (c) the longitudinal anti-bonding rim mode (1.420 eV); and (d) a transverse rim mode (1.772 eV). (e) SEM image of SRR; (f-h) SPR maps extracted from CL data showing (f) the longitudinal bonding and (g) anti-bonding rim modes; and (h) a transverse rim mode; (i) EELS and CL spectra, insets indicate the areas from which the spectra were extracted.

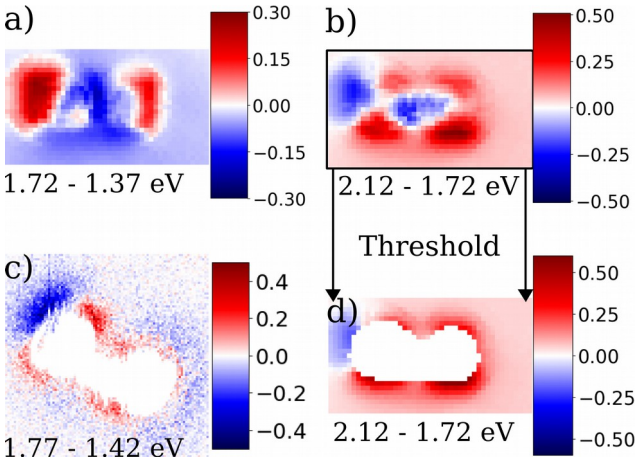

Figure 6: Difference maps of neighbouring peaks, as seen in the spectra and extracted energy slices available in Figure 5. (a) CL difference map between the longitudinal bonding mode (1.375 eV, blue) subtracted from the longitudinal anti-bonding rim mode (1.725 eV, red); (b) CL difference map between longitudinal anti-bonding rim mode (1.725 eV, blue) subtracted from transverse rim mode (2.120 eV, red); (c) EELS difference map of longitudinal anti-bonding mode (1.420 eV blue) subtracted from transverse mode (1.772 eV, red); (d) repetition of (b) with pixels corresponding to the physical sample removed for a clear comparison with the same modes in the EELS data (c).